SCIENTIFIC REPORTS

OPEN

A Revisit to High Thermoelectric Performance of Single-layer MoS_2

Zelin Jin[1,2,*], Quanwen Liao[3,*], Haisheng Fang[1,2], Zhichun Liu[3], Wei Liu[3], Zhidong Ding[2], Tengfei Luo[4] & Nuo Yang[1,2]

Received: 14 June 2015
Accepted: 16 November 2015
Published: 17 December 2015

Both electron and phonon transport properties of single layer MoS_2 ($SLMoS_2$) are studied. Based on first-principles calculations, the electrical conductivity of $SLMoS_2$ is calculated by Boltzmann equations. The thermal conductivity of $SLMoS_2$ is calculated to be as high as 116.8 $Wm^{-1}K^{-1}$ by equilibrium molecular dynamics simulations. The predicted value of *ZT* is as high as 0.11 at 500 K. As the thermal conductivity could be reduced largely by phonon engineering, there should be a high possibility to enhance *ZT* in the $SLMoS_2$-based materials.

Thermoelectric materials are essential for converting waste heat to electricity and solid-state cooling, which have attracted much attention recently[1–10]. The dimensionless figure of merit (ZT) is utilized to evaluate the efficiency of the thermoelectric conversion, defined as: $ZT = S^2\sigma T/\kappa$, where S is the Seebeck coefficient, σ is the electrical conductivity, T is the absolute temperature, and κ is the total thermal conductivity. The κ is composed of electrons' contribution (κ_e) and phonons' contribution (κ_p). The ZT value for most commercial materials are around one, which is far below the critical value of three that is comparable with the traditional energy conversion in efficiency[3]. In the past two decades, nano-materials and nano-structured materials are expected to have excellent energy conversion efficiency due to the higher power factor ($S^2\sigma$)[11,12] and lower κ_p[13–15], which are also known as the electron-crystal and phonon-glass.

The graphene, as the first two dimensional material, has extraordinary electronic property as well as super high thermal conductivity[16]. However, the pristine graphene, a semi-metal, has zero band gap and very small S[17]. Different from graphene, single layer MoS_2 ($SLMoS_2$) is a semiconductor and has a direct band-gap[18], which enables its wide applications in electronic and optical devices, such as field effect transistor[19].

Recently, some works have studied the electronic and phononic properties of $SLMoS_2$. Eugene *et al.* have calculated the electronic structure of $SLMoS_2$ which is compared with that of bulk MoS_2[20], and revealed the transition mechanism from the direct band gap of $SLMoS_2$ to the indirect band gap of bulk MoS_2. Emilio *et al.* have shown that, after applying compressive or tensile bi-axial strain, the electronic structure of $SLMoS_2$ transitions from semiconductor to metal[21]. Li *et al.* calculated the intrinsic electrical transport and electron-phonon interaction properties of $SLMoS_2$[22]. Moreover, the thermoelectric potential of $SLMoS_2$ has been explored and a maximum ZT, at room temperature, is obtained as 0.5 by Huang *et al.*[23] using the ballistic model. The scatterings of electrons are not considered in their ballistic model, which should have led to an over-estimation of ZT. Fu *et al.* studied $SLMoS_2$ ribbons and calculated the ZT value to be up to 3.4[24]. Besides theoretical predictions, Wu *et al.* has experimentally reported a value of S as 30 mV/K for $SLMoS_2$[25], which indicates an appealing potential for thermoelectric applications.

Besides electron properties, some works focused on the phonon properties of $SLMoS_2$. The $SLMoS_2$ nanoribbon has a low thermal conductivity due to the size effect. Jiang *et al.* claimed that κ_p of $SLMoS_2$ nanoribbon was around 5 $Wm^{-1}K^{-1}$ at room temperature by molecular dynamics (MD) simulations[26]. Zhang *et al.* reported three results for $SLMoS_2$ nanoribbons which were 1.35 $Wm^{-1}K^{-1}$ by equilibrium molecular dynamics (EMD)[27], 23.2 $Wm^{-1}K^{-1}$ by non-equilibrium Green's function[28], and 26.2 $Wm^{-1}K^{-1}$ by Boltzmann transport equation[29]. However, there are also reports on the thermal conductivities for MoS_2 with higher values. Li *et al.* predicts the κ as 83 $Wm^{-1}K^{-1}$ from *ab initio* calculations[30]. With high-quality sample, the κ of suspended few layers MoS_2 has been measured as 52 $Wm^{-1}K^{-1}$ [31] and 35 $Wm^{-1}K^{-1}$ [32]. Liu *et al.* claimed that the basal-plane thermal conductivity

[1]State Key Laboratory of Coal Combustion, Huazhong University of Science and Technology (HUST), Wuhan 430074, People's Republic of China. [2]Nano Interface Center for Energy (NICE), School of Energy and Power Engineering, Huazhong University of Science and Technology (HUST), Wuhan 430074, People's Republic of China. [3]School of Energy and Power Engineering, Huazhong University of Science and Technology (HUST), Wuhan 430074, People's Republic of China. [4]Department of Aerospace and Mechanical Engineering, University of Notre Dame, Notre Dame, Indiana 46556, USA. *These authors contributed equally to this work. Correspondence and requests for materials should be addressed to N.Y. (email: nuo@hust.edu.cn) or H.F. (email: hafang@hust.edu.cn) or Z.L. (email: zcliu@hust.edu.cn)

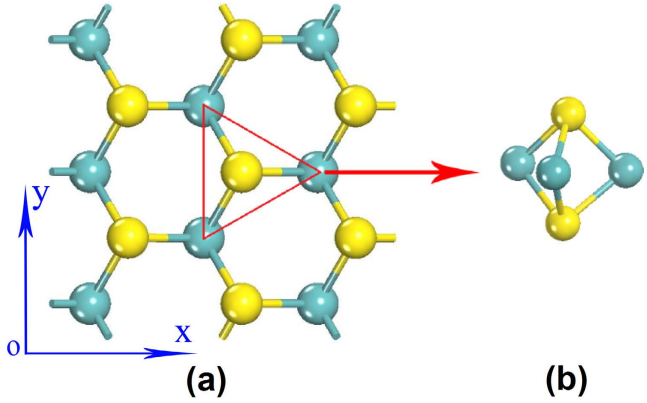

Figure 1. The structure of single layer MoS_2. (**a**) The top view, a hexagonal lattice structure. (**b**) The side view of the inset triangle. Each sulfur atom has three molybdenum atoms as its first nearest neighbor atom. Each molybdenum atom has six sulfur atoms as its first nearest neighbor atom.

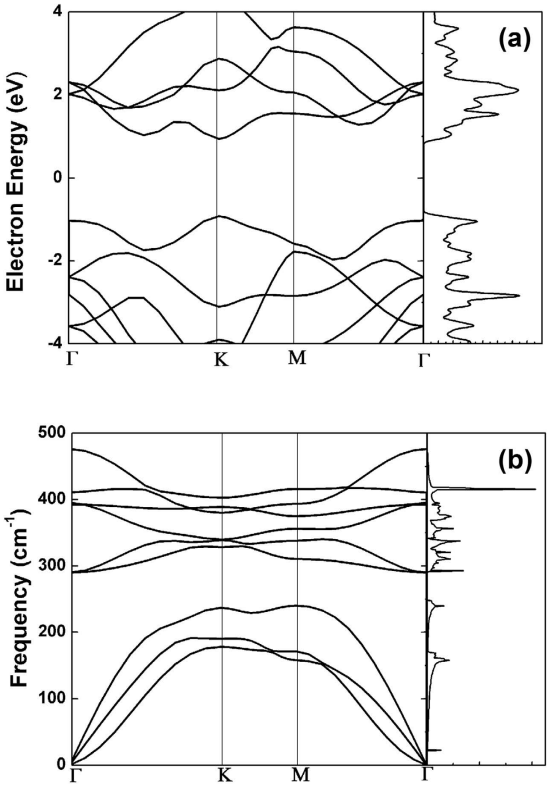

Figure 2. (**a**) Electron band structure and density of state along the symmetry line. The Fermi energy is set in the middle of the gap. (**b**) The phonon dispersion for $SLMoS_2$ and the phonon density of state in the whole Brillouin zone.

of single crystal MoS_2 would be 85–110 $Wm^{-1}K^{-1}$ [33]. There is not an agreement on the κ of $SLMoS_2$, and it needs more works on this issue.

In this paper, both electron and phonon transport properties of $SLMoS_2$ are studied (the structure as shown in Fig. 1). Based on the electronic band structure from first-principles calculations, the electrical conductivity of $SLMoS_2$ is calculated by Boltzmann equations. Both the electronic structure and phonon dispersion relation are calculated. Together with κ_p calculated from classical EMD simulations, the thermoelectric properties are obtained. The results show that $SLMoS_2$ is a promising material for thermoelectric engineering.

Results and Discussions

The electronic band structure of $SLMoS_2$ along the high-symmetry points in Brillouin zone is shown in Fig. 2(a). At the K point, there is a direct band gap as 1.86 eV which agrees well with previous calculations (1.69 ~ 1.98 eV)[20–23,34,35]. Another characteristic in the $SLMoS_2$ band structure is that there is a Q valley along the Γ-K path. The Q valley

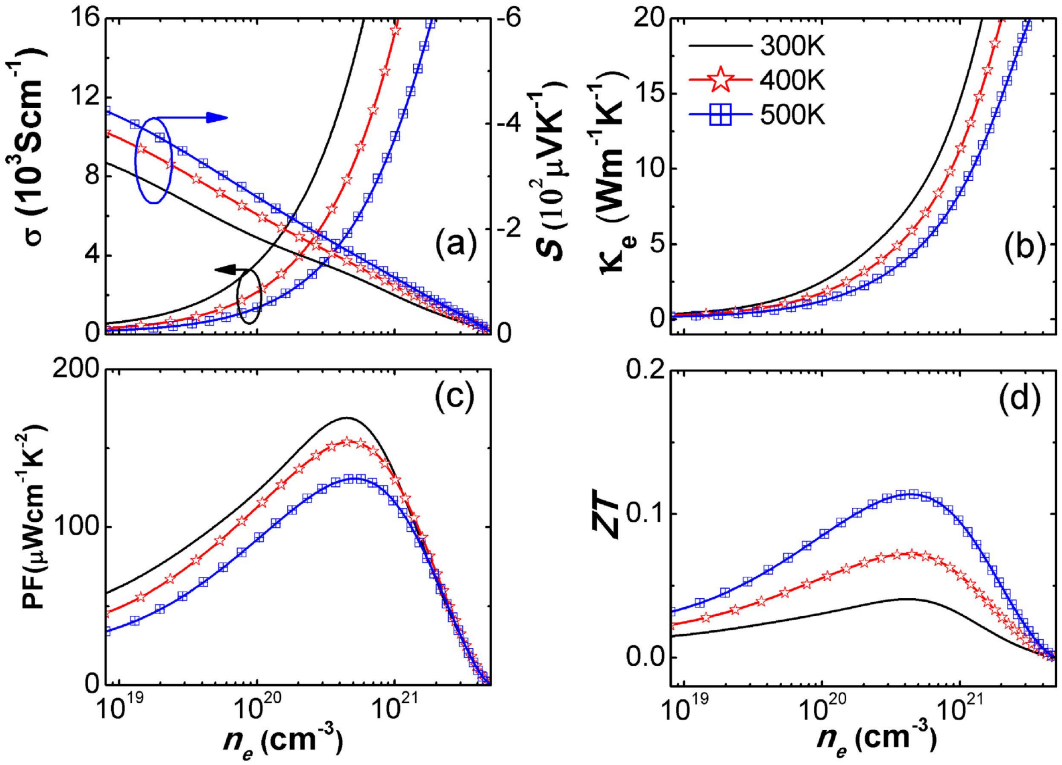

Figure 3. The thermoelectric transport properties of n-type $SLMoS_2$ at 300K, 400K and 500K. (**a**) The electrical conductivity and Seebeck coefficient; (**b**) The electrical thermal conductivity; (**c**) The power factor; (**d**) The figure of merit. The thermoelectric transport properties of p-type is shown in supporting information.

yields a larger effective mass than the K valley, which leads to strong electron-phonon interactions in MoS_2 at this point[22]. The large effective mass of carriers and multi-valleys band structure are favorable for a high ZT[36]. As shown in the density of state (DOS) electrons (Fig. 2), there are sharp gradients at the edges of both conduction and valence band and several peaks near band edges, due to the quantum size effects in the 2D structure, which may enhance ZT as the prediction of Mahan and Sofo[12].

We made a full calculation of the thermoelectric properties of $SLMoS_2$ at 300 K, 400 K and 500 K. As shown in Fig. 3(a,b), κ_e and σ increase as the increasing of carrier concentration (n_e). When the Fermi level is in the band gap, n_e and σ is much smaller. As the Fermi level moves up into the conduction band, n_e and σ increases quickly (more details shown in Fig. S4 and S6 in supporting information). Shown in Fig. 3(a), the Seebeck coefficient has a large value and decreases with the increase of n_e. The Fermi level for ZT peak locates around the first DOS peak, and this is consistent with the prediction that a delta DOS would result in an optimum ZT[12]. It leads to a power factor as high as several hundreds of $\mu Wcm^{-1}K^{-2}$ (shown in Fig. 3(c)), which is compared with those of high ZT thermoelectric materials, such as BiTe[37] and PbTe[38].

The phonon dispersion relation of $SLMoS_2$ is also calculated and shown in Fig. 2(b). In the vicinity of Γ point, the out-of-plane transverse acoustic branch (ZA) has a quadratic relation, both the transversal acoustic branch (TA) and longitudinal acoustic branch (LA) have linear relations. The group velocities at Γ point along Γ-M direction are around 667.5 m/s (TA) and 1080.2 m/s (LA), which are much smaller than the group velocities in graphene[39], as 3743 m/s (TA) and 5953 m/s (LA).

For semiconductors, the thermal conductivity is mainly contributed by phonons (κ_p). We calculated κ_p by EMD and show in Fig. 4. The κ_p of $SLMoS_2$ exhibits a size dependence on the simulation cell and reaches a converged value when the simulation cell is larger than $8 \times 8 \times 1$ units^3 ($8.66 \times 7.50 \times 0.616\,nm^3$) (Fig. 4(a)). A weak anisotropy is observed in thermal conductivities along armchair and zigzag direction. The average value of κ_p along armchair and zigzag directions is $116.8\,Wm^{-1}K^{-1}$ for simulation cell as large as $32 \times 32 \times 1$ units^3 ($34.7 \times 30.0 \times 0.616\,nm^3$) at 300K. In Fig. 4(b), the κ_p of $SLMoS_2$ decreases with the increasing temperature ($79.6\,Wm^{-1}K^{-1}$ and $52.9\,Wm^{-1}K^{-1}$ at 400 K and 500 K, respectively), because there are more three phonon Umklapp scatterings for high temperature. A lower κ_p is good for enhancing thermoelectric properties.

Comparing with previous results (details in Table 1), we obtained a maximum value of κ_p of $SLMoS_2$. Some of these works focused on the $SLMoS_2$ nanoribbons[26,27,29] which have very low thermal conductivities, because the phonon confinement effect in nanostructures[40,41]. Using the same empirical potential in MD simulations, our results for $SLMoS_2$ is around 20 times larger than that of nanoribbon with $34.6 \times 30 \times 0.61\,nm^3$ in size. Besides, due to the interlayer coupling by van Der Waals forces[42], the multilayer structures[31,33] should be lower than the single layer[27,28,30,32] in thermal conductivity. Due to the absence of impurities, defects and interlayer scatterings in MD simulations, the κ_p of $SLMoS_2$ is a little higher than the measurements of bulk multilayer $SLMoS_2$[33], 85 ~ 110 $Wm^{-1}K^{-1}$. Our value is comparable to the result predicted from *ab initio* calculation[30] , where stated that the lower bound

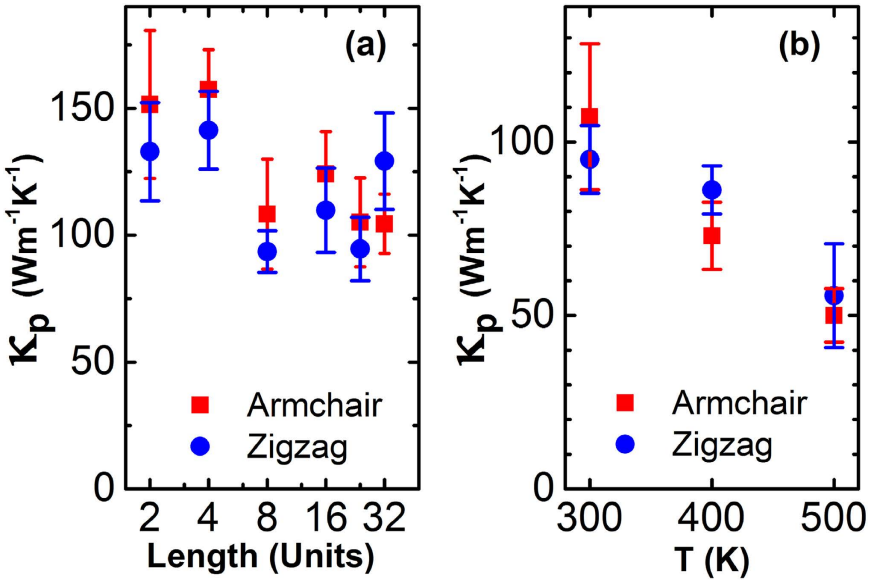

Figure 4. (**a**) The dependence of thermal conductivity (κ_p) of $SLMoS_2$ upon the size of simulation cell. The size of simulation cell size equals the length (L) times a supercell ($1.083 \times 0.938 \times 0.616\,nm^3$). (**b**) The thermal conductivity of $SLMoS_2$ for three different temperature as 300K, 400K and 500K, respectively.

Struct.& Ref.	Method	T (K)	Carrier type	σ (Scm^{-1})	S (μVK^{-1})	κ_e ($Wm^{-1}K^{-1}$)	κ_{ph} ($Wm^{-1}K^{-1}$)	ZT
SL	DFT + BTE + MD	300	n	14625	−110	8.94	116.8	0.04
			p	16957	72.9	11.39		0.02
		500	n	11714	−161	9.69	52.9	0.26
			p	8853	150	8.40		0.16
SL[23]	DFT + Ballistic model	300	n	54	−202	0.021	0.243	0.25
			p	108	215	0.040	0.244	0.53
SLR[24,27]	DFT + BTE + MD	300	n	7770	−204	2.89	1.02	2.5
			p	14300	223	5.20		3.4
SL CVD[25]	Experiment	300	–	–	≤30000	–	–	–
SL FET[59]	Experiment	300	–	–	400–100000	–	–	–
Bulk[60]	Experiment	90–873	–	–	500–700	–	–	–
SL[27]	EMD	300	–	–	–	–	1.35	–
SL[30]	DFT + BTE		–	–	–	–	>83	–
SL[28]	DFT + NEGF		–	–	–	–	23.2	–
SLR[29]	DFT + BTE		–	–	–	–	26.2	–
SLR[26]	NEMD		–	–	–	–	5	–
FL[31]	Experiment		–	–	–	–	52	–
SL[32]	Experiment		–	–	–	–	35.4	–
Bulk[33]	Experiment		–	–	–	–	85– 110	–

Table 1. The comparison of thermoelectric properties for different MoS_2 structures, including single layer (SL), few layers (FL), single layer ribbon (SLR), and bulk MoS_2.

of κ_p as 83 $Wm^{-1}K^{-1}$ at 300 K in the considering of phonon scatters and the simplification in calculation of BTE model. Another advantage for our results is that both the nonequilibrium Green's function calculation[28] and the Boltzmann transport equation[29] adopt artificial relaxation time approximations for phonon-phonon Umklapp scatterings, which is not required in the MD simulations.

Generally, there are two types of commonly used MD simulation methods, EMD and non-equilibrium MD (NEMD). The EMD is better than NEMD in predicting a bulk structure by applying the periodic boundary condition, because NEMD need impose artificial heat bath and use the extrapolating method. However, NEMD gets the advantage of EMD in predicting a structure with a finite size. There is a EMD report which showed a low value of κ_p of $SLMoS_2$ as 1.35 $Wm^{-1}K^{-1}$ [27]. The potential functions used in Ref. [27] are determined by tight-binding

quantum chemistry calculations and used to reproduce the crystal structure and Raman spectrum. The empirical potential function is important to obtain a reliable value of thermal conductivity. Differently, the Stillinger-Weber potential[26] ,used in this work, can reproduce a better phonon dispersion relations, which will describe the heat transfer properties with a better reliability (details in supporting information).

With the above calculations of electron and phonon properties, *ZT* profiles can be obtained and are shown in Fig. 3(d). There is a parabolic tendency for *ZT* in the whole carrier concentration range. The optimized *ZT* values are 0.04, 0.07, and 0.11 for 300 K, 400 K and 500 K, respectively. These values get bigger as temperature increases because of the improved power factors and the reduced thermal conductivity. These optimized *ZT* values correspond to the situations where the Fermi level moves up to the first peak in the conduction band.

As shown in Table 1, we list some recently results on thermoelectric properties of different $SLMoS_2$ structures. The value of *ZT* is in the same order of Ref. [23] and one order smaller than that of $SLMoS_2$ ribbon. Our results of κ_p is higher than others. As shown in Fig. 4(a), our results of κ_p overcome the size confinement effect and corresponds to an infinite $SLMoS_2$ sheet. Moreover, different from NEMD, it does not need the assumption of linear relationship between $1/\kappa_p$ and 1/L.

Compared to nanoporous silicon analyzed by Lee[43], we get the similar *ZT* trend and magnitude of these transport values. As shown in Fig. 3(c), the power factor of $SLMoS_2$ is larger than that of nanoporous silicon. The large power factor of $SLMoS_2$ comes from a larger intrinsic σ and a comparable *S*. It indicates that the $SLMoS_2$ has comparable electron properties as the optimized nanoporous silicon. However, due to the high κ_e and κ_p, the $SLMoS_2$ has a modest *ZT* value. It is also worth noting that the *ZT* value here is smaller than the prediction from ballistic models by Huang *et al.* where neglects the phonon scatterings[23].

Although the predicted *ZT* value of $SLMoS_2$ is not over one, $SLMoS_2$-based materials may be a good candidate for thermoelectric application. Our results show that $SLMoS_2$ has a much higher thermal conductivity (~116 $Wm^{-1}K^{-1}$, at 300 K) than other thermoelectric materials (on the order of 1 $Wm^{-1}K^{-1}$)[6,44]. The higher thermal conductivity makes a bigger room for thermal conductivity reduction by phonon engineering. There are some conventional ways to reduce thermal conductivity by phonon engineering, such as isotope doping[45], nanoporous structure[14,43,46,47], nanoribbons[48], or folding[49] etc. The mechanism is to introduce more phonon scatterings which can shorten phonon mean free paths. For example, bulk silicon has a *ZT* value as low as 0.003. Then, with phonon engineering, Si-based nanomaterials, such as Si nanowires[45,50], nanoporous Si[14,43,46,47], and nanostructured Si[51], may reach a two orders larger *ZT*. Another inspiration example is the graphene. The high pristine thermal conductivity of graphene can be reduced largely by phonon engineering[48,49,52] which make a *ZT* as high as 3[52].

The values of *ZT* and power factor of $SLMoS_2$ are much higher than those of silicon and graphene. With a reduced thermal conductivity and kept electron transport properties, the values of *ZT* of SLMoS2-based materials may be larger than one. Generally, a side-effect of phonon engineering is the reduction of power factor. However, the side-effect is not obvious because the mean free paths of electrons are around two orders smaller than that of phonons, such as what is shown in the recent thermoelectric results on Si phononic crystals[47].

Conclusion

The thermoelectric properties of $SLMoS_2$ are explored using theoretical calculations. The electronic structure and phonon dispersion relation are calculated using DFT calculations. Combined with molecule dynamics simulations and Boltzmann equations, thermoelectric properties are predicted as a function of carrier concentration at room temperature. With the lattice thermal conductivity as 116.8 $Wm^{-1}K^{-1}$, 79.6 $Wm^{-1}K^{-1}$, and 52.9 $Wm^{-1}K^{-1}$, the optimized *ZT* of $SLMoS_2$ is found to be of 0.04, 0.07 and 0.11 at 300 K, 400 K and 500 K, respectively. As $SLMoS_2$ has a higher *ZT* than other pristine structure, like silicon and graphene, there will be a big room to enhance *ZT* in $SLMoS_2$-based materials by the developing phonon-engineering.

Methods

To calculate electronic properties, the first-principles calculation is implemented by QUANTUM ESPRESSO in the frame of density functional theory (DFT)[53]. The local density approximation (LDA) is used in the exchange-correlation approximation while the semi-core valence for molybdenum is considered with the Goedecker-Hartwigsen-Hutter-Tetter method[54]. The wave-functions in electronic calculation are cut off at 160 Ry, and the irreducible Brillouin zone is sampled with a $16 \times 16 \times 1$ Monkhorst-Pack grid.

The hexagon primitive cell is used to structure relaxation and property prediction in DFT calculation. Structure relaxation for $SLMoS_2$ yields lattice constant of about 3.13 Å, consistent with previous predictions of 3.12–3.16 Å[20–22]. For the consistency of property evaluation, the thickness of $SLMoS_2$ is assumed to be 6.16 Å – the same as that of the single-sheet in bulk MoS_2[55]. The calculations on both electrons and phonons are based on this optimized structure.

In the calculations of transport coefficients, a k-point mesh as $28 \times 28 \times 1$ (denser enough to obtain converged results) is used over the irreducible Brillouin zone. With the assumption of constant relaxation time, the transport coefficient for electrons can be calculated using BoltzTrap[56] which solves Boltzmann transport equation (more details in supporting information).

The thermal conductivity of $SLMoS_2$, κ_p, is calculated by EMD with the Green-Kubo approach[57]. All the simulations are carried out utilizing the LAMMPS software package[58]. The Stillinger-Weber potential with parameters fitted by Jiang *et al.*[26] is adopted in our simulations. The $SLMoS_2$ film is constructed by periodic arrangement of supercell illustrated in Fig. 1, and the sizes of $1 \times 1 \times 1$ $units^3$ supercell corresponds to $1.083 \times 0.938 \times 0.616$ nm^3. To study the finite size effect on thermal conductivities, we calculated the simulation cells with the volumes from $2 \times 2 \times 1$ to $32 \times 32 \times 1$ $units^3$ at room temperature (more details in supporting information).

References

1. Chen, B. J., Sun, X. W. & Xu, C. Fabrication of zinc oxide nanostructures on gold-coated silicon substrate by thermal chemical reactions vapor transport deposition in air. Ceram Int 30, 1725–1729, doi: 10.1016/j.ceramint.2003.12.140 (2004).

2. Vineis, C. J., Shakouri, A., Majumdar, A. & Kanatzidis, M. G. Nanostructured Thermoelectrics: Big Efficiency Gains from Small Features. *Adv. Mat.* **22,** 3970–3980, doi: 10.1002/adma.201000839 (2010).
3. Shakouri, A. Recent Developments in Semiconductor Thermoelectric Physics and Materials. *Annu Rev Mater Res* **41,** 399–431, doi: 10.1146/annurev-matsci-062910-100445 (2011).
4. Vaqueiro, P. & Powell, A. V. Recent developments in nanostructured materials for high-performance thermoelectrics. *J. Mater. Chem.* **20,** 9577–9584, doi: 10.1039/c0jm01193b (2010).
5. Sootsman, J. R., Chung, D. Y. & Kanatzidis, M. G. New and Old Concepts in Thermoelectric Materials. *Angew. Chem.-Int. Edit.* **48,** 8616–8639, doi: 10.1002/anie.200900598 (2009).
6. Minnich, A. J., Dresselhaus, M. S., Ren, Z. F. & Chen, G. Bulk nanostructured thermoelectric materials: current research and future prospects. *Energy Environ. Sci.* **2,** 466–479, doi: 10.1039/b822664b (2009).
7. Snyder, G. J. & Toberer, E. S. Complex thermoelectric materials. *Nat. Mater.* **7,** 105–114, doi: 10.1038/nmat2090 (2008).
8. Dresselhaus, M. S. *et al.* New Directions for Low-Dimensional Thermoelectric Materials. *Adv. Mat.* **19,** 1043–1053, doi: 10.1002/adma.200600527 (2007).
9. Nolas, G. S., Poon, J. & Kanatzidis, M. Recent developments in bulk thermoelectric materials. *Mrs Bulletin* **31,** 199–205, doi: 10.1557/Mrs2006.45 (2006).
10. Martín-González, M., Caballero-Calero, O. & Díaz-Chao, P. Nanoengineering thermoelectrics for 21st century: Energy harvesting and other trends in the field. *Renew. Sust. Energ. Rev.* **24,** 288–305, doi: 10.1016/j.rser.2013.03.008 (2013).
11. Hicks, L. D. & Dresselhaus, M. S. Effect of quantum-well structures on the thermoelectric figure of merit. *Phys. Rev. B* **47,** 12727–12731, doi: 10.1103/PhysRevB.47.12727 (1993).
12. Mahan, G. D. & Sofo, J. O. The best thermoelectric. *Proceedings of the National Academy of Sciences* **93,** 7436–7439, doi: 10.1073/pnas.93.15.7436 (1996).
13. Jiang, J. W., Yang, N., Wang, B. S. & Rabczuk, T. Modulation of thermal conductivity in kinked silicon nanowires: phonon interchanging and pinching effects. *Nano Lett.* **13,** 1670–1674, doi: 10.1021/nl400127q (2013).
14. Yang, L., Yang, N. & Li, B. Extreme low thermal conductivity in nanoscale 3D Si phononic crystal with spherical pores. *Nano Lett.* **14,** 1734–1738, doi: 10.1021/nl403750s (2014).
15. Poudel, B. *et al.* High-thermoelectric performance of nanostructured bismuth antimony telluride bulk alloys. *Science* **320,** 634–638, doi: 10.1126/science.1156446 (2008).
16. Balandin, A. A. Thermal properties of graphene and nanostructured carbon materials. *Nat Mater* **10,** 569–581, doi: 10.1038/nmat3064 (2011).
17. Zuev, Y. M., Chang, W. & Kim, P. Thermoelectric and magnetothermoelectric transport measurements of graphene. *Phys Rev Lett* **102,** 096807, doi: 10.1103/PhysRevLett.102.096807 (2009).
18. Mak, K. F., Lee, C., Hone, J., Shan, J. & Heinz, T. F. Atomically Thin MoS2: A New Direct-Gap Semiconductor. *Phys. Rev. Lett.* **105,** 136805, doi: 10.1103/PhysRevLett.105.136805 (2010).
19. Radisavljevic, B., Radenovic, A., Brivio, J., Giacometti, V. & Kis, A. Single-layer MoS2 transistors. *Nat Nanotechnol* **6,** 147–150, doi: 10.1038/nnano.2010.279 (2011).
20. Kadantsev, E. S. & Hawrylak, P. Electronic structure of a single MoS2 monolayer. *Solid State Commun.* **152,** 909–913, doi: 10.1016/j.ssc.2012.02.005 (2012).
21. Scalise, E., Houssa, M., Pourtois, G., Afanas'ev, V. V. & Stesmans, A. Strain-induced semiconductor to metal transition in the two-dimensional honeycomb structure of MoS2. *Nano Res* **5,** 43–48, doi: 10.1007/s12274-011-0183-0 (2012).
22. Li, X. D. *et al.* Intrinsic electrical transport properties of monolayer silicene and MoS2 from first principles. *Phys. Rev. B* **87,** 115418, doi: 10.1103/PhysRevB.87.115418 (2013).
23. Huang, W., Da, H. X. & Liang, G. C. Thermoelectric performance of MX2 (M = Mo,W; X = S, Se) monolayers. *J. Appl. Phys.* **113,** 104304, doi: 10.1063/1.4794363 (2013).
24. Fan, D. D. *et al.* MoS2 nanoribbons as promising thermoelectric materials. *Appl. Phys. Lett.* **105,** 133113, doi: 10.1063/1.4897349 (2014).
25. Wu, J. *et al.* Large thermoelectricity via variable range hopping in chemical vapor deposition grown single-layer MoS2. *Nano Lett.* **14,** 2730–2734, doi: 10.1021/nl500666m (2014).
26. Jiang, J. W., Park, H. S. & Rabczuk, T. Molecular dynamics simulations of single-layer molybdenum disulphide (MoS2): Stillinger-Weber parametrization, mechanical properties, and thermal conductivity. *J. Appl. Phys.* **114,** 064307, doi: 10.1063/1.4818414 (2013).
27. Liu, X. J., Zhang, G., Pei, Q. X. & Zhang, Y. W. Phonon thermal conductivity of monolayer MoS2 sheet and nanoribbons. *Appl. Phys. Lett.* **103,** 133113, doi: 10.1063/1.4823509 (2013).
28. Cai, Y., Lan, J., Zhang, G. & Zhang, Y.-W. Lattice vibrational modes and phonon thermal conductivity of monolayer MoS2. *Phys. Rev. B* **89,** 035438, doi: 10.1103/PhysRevB.89.035438 (2014).
29. Wei, X. *et al.* Phonon thermal conductivity of monolayer MoS2: A comparison with single layer graphene. *Appl. Phys. Lett.* **105,** 103902, doi: 10.1063/1.4895344 (2014).
30. Li, W., Carrete, J. & Mingo, N. Thermal conductivity and phonon linewidths of monolayer MoS2 from first principles. *Appl. Phys. Lett.* **103,** 253103, doi: 10.1063/1.4850995 (2013).
31. Sahoo, S., Gaur, A. P. S., Ahmadi, M., Guinel, M. J. F. & Katiyar, R. S. Temperature-Dependent Raman Studies and Thermal Conductivity of Few-Layer MoS2. *J. Phys. Chem. C* **117,** 9042–9047, doi: 10.1021/jp402509w (2013).
32. Yan, R. *et al.* Thermal conductivity of monolayer molybdenum disulfide obtained from temperature-dependent Raman spectroscopy. *ACS Nano* **8,** 986–993, doi: 10.1021/nn405826k (2014).
33. Liu, J., Choi, G. M. & Cahill, D. G. Measurement of the anisotropic thermal conductivity of molybdenum disulfide by the time-resolved magneto-optic Kerr effect. *J. Appl. Phys.* **116,** 233107, doi: 10.1063/1.4904513 (2014).
34. Molina-Sánchez, A. & Wirtz, L. Phonons in single-layer and few-layer MoS2and WS2. *Phys. Rev. B* **84,** 155413, doi: 10.1103/PhysRevB.84.155413 (2011).
35. Kaasbjerg, K., Thygesen, K. S. & Jacobsen, K. W. Phonon-limited mobility in n-type single-layer MoS2 from first principles. *Phys. Rev. B* **85,** 115317, doi: 10.1103/PhysRevB.85.115317 (2012).
36. Pei, Y. *et al.* Convergence of electronic bands for high performance bulk thermoelectrics. *Nature* **473,** 66–69, doi: 10.1038/nature09996 (2011).
37. Poudel, B. *et al.* High-thermoelectric performance of nanostructured bismuth antimony telluride bulk alloys. *Science* **320,** 634–638, doi: 10.1126/science.1156446 (2008).
38. Biswas, K. *et al.* High-performance bulk thermoelectrics with all-scale hierarchical architectures. *Nature* **489,** 414–418, doi: 10.1038/nature11439 (2012).
39. Ong, Z.-Y. & Pop, E. Effect of substrate modes on thermal transport in supported graphene. *Phys. Rev. B* **84,** 075471, doi: 10.1103/PhysRevB.84.075471 (2011).
40. Yang, N., Zhang, G. & Li, B. Violation of Fourier's law and anomalous heat diffusion in silicon nanowires. *Nano Today* **5,** 85–90, doi: 10.1016/j.nantod.2010.02.002 (2010).
41. Volz, S. G. & Chen, G. Molecular dynamics simulation of thermal conductivity of silicon nanowires. *Appl. Phys. Lett.* **75,** 2056, doi: 10.1063/1.124914 (1999).
42. Chen, J., Zhang, G. & Li, B. Substrate coupling suppresses size dependence of thermal conductivity in supported graphene. *Nanoscale* **5,** 532–536, doi: 10.1039/c2nr32949b (2013).

43. Lee, J.-H., Galli, G. A. & Grossman, J. C. Nanoporous Si as an efficient thermoelectric material. *Nano Lett.* **8,** 3750–3754, doi: 10.1021/nl802045f (2008).
44. He, J., Kanatzidis, M. G. & Dravid, V. P. High performance bulk thermoelectrics via a panoscopic approach. *Materials Today* **16,** 166–176, doi: 10.1016/j.mattod.2013.05.004 (2013).
45. Yang, N., Gang, Z. & Li, B. Ultralow Thermal Conductivity of Isotope-Doped Silicon Nanowires. *Nano Lett.* **8,** 276–280, doi: 10.1021/nl0725998 (2007).
46. Tang, J. Y. *et al.* Holey Silicon as an Efficient Thermoelectric Material. *Nano Lett.* **10,** 4279–4283, doi: 10.1021/Nl102931z (2010).
47. Yang, L., Yang, N. & Li, B. Thermoelectric Properties of Nanoscale three dimensional Si Phononic Crystal. *arXiv preprint arXiv:1410.8193* (2014).
48. Liang, L., Cruz-Silva, E., Girao, E. C. & Meunier, V. Enhanced thermoelectric figure of merit in assembled graphene nanoribbons. *Phys. Rev. B* **86,** 115438, doi: 10.1103/PhysRevB.86.115438 (2012).
49. Yang, N., Ni, X., Jiang, J.-W. & Li, B. How does folding modulate thermal conductivity of graphene? *Appl. Phys. Lett.* **100,** 093107, doi: 10.1063/1.3690871 (2012).
50. Vo, T. T., Williamson, A. J., Lordi, V. & Galli, G. Atomistic design of thermoelectric properties of silicon nanowires. *Nano Lett.* **8,** 1111–1114, doi: 10.1021/nl073231d (2008).
51. Bux, S. K. *et al.* Nanostructured Bulk Silicon as an Effective Thermoelectric Material. *Adv. Funct. Mater.* **19,** 2445–2452, doi: 10.1002/adfm.200900250 (2009).
52. Chang, P. H., Bahramy, M. S., Nagaosa, N. & Nikolic, B. K. Giant Thermoelectric Effect in Graphene-Based Topological Insulators with Heavy Adatoms and Nanopores. *Nano Lett.* **14,** 3779–3784, doi: Doi 10.1021/Nl500755m (2014).
53. Giannozzi, P. *et al.* Quantum Espresso: a modular and open-source software project for quantum simulations of materials. *J. Phys. Condens. Mat.* **21,** 395502, doi: 10.1088/0953-8984/21/39/395502 (2009).
54. Hartwigsen, C., Goedecker, S. & Hutter, J. Relativistic separable dual-space Gaussian pseudopotentials from H to Rn. *Phys. Rev. B* **58,** 3641–3662, doi: 10.1103/PhysRevB.58.3641 (1998).
55. Villars, P. *et al.* SpringerMaterials; sm_lbs_978-3-540-32682-3_19 (Springer-Verlag GmbH, Heidelberg, 2006), http://materials.springer.com/lb/docs/sm_lbs_978-3-540-32682-3_19 doi: 10.1007/10920503_19.
56. Madsen, G. K. H. & Singh, D. J. BoltzTraP. A code for calculating band-structure dependent quantities. *Comput Phys Commu* **175,** 67–71, doi: 10.1016/j.cpc.2006.03.007 (2006).
57. Hoover, W. G. *et al.* Lennard-Jones triple-point bulk and shear viscosities. Green-Kubo theory, Hamiltonian mechanics, and nonequilibrium molecular dynamics. *Phys. Rev. A* **22,** 1690–1697, doi: 10.1103/PhysRevA.22.1690 (1980).
58. Plimpton, S. Fast Parallel Algorithms for Short-Range Molecular Dynamics. *J. Comput. Phys.* **117,** 1–19, doi: 10.1006/jcph.1995.1039 (1995).
59. Buscema, M. *et al.* Large and tunable photothermoelectric effect in single-layer MoS2. *Nano Lett.* **13,** 358–363, doi: 10.1021/nl303321g (2013).
60. Mansfield, R. & Salam, S. Electrical properties of molybdenite. *Proceedings of the Physical Society. Section B* **66,** 377, doi: 10.1088/0370-1301/66/5/305 (1953).

Acknowledgements

This project was supported in part by the grants from the National Natural Science Foundation of China: 51476068 (H.F.), 51576076(N.Y.), and 51376069 (Z.L.) and the Major State Basic Research Development Program of China 2013CB228302 (Z.L.). The authors are grateful to Lina Yang and Jing-Tao Lű for useful discussions. The authors thank the National Supercomputing Center in Tianjin (NSCC-TJ) for providing help in computations.

Author Contributions

Z.J. and Z.D. carried out the first-principles calculations. Q.L. carried out the MD calculations. N.Y., Z.J., Q.L. and Z.D. analyzed the calculation data. H.F., Z.L., W.L. and T.L. discussed and commented on the manuscript. Z.J., Q.L., Z.D. and N.Y. edited the manuscript. N.Y., H.F. and Z.L. supervised the research.

Additional Information

Competing financial interests: The authors declare no competing financial interests.

How to cite this article: Jin, Z. *et al.* A Revisit to High Thermoelectric Performance of Single-layer MoS_2. *Sci. Rep.* **5**, 18342; doi: 10.1038/srep18342 (2015).

Supporting Information

A Revisit to High Thermoelectric Performance of Single-layer MoS_2

Zelin Jin[1,2, #], Quanwen Liao[3, #], Haisheng Fang[1,2,*], Zhichun Liu[3,*], Wei Liu[3], Zhidong Ding[2], Tengfei Luo[4], Nuo Yang[1,2,*]

[1] State Key Laboratory of Coal Combustion, Huazhong University of Science and Technology (HUST), Wuhan 430074, People's Republic of China

[2] Nano Interface Center for Energy (NICE), School of Energy and Power Engineering, Huazhong University of Science and Technology (HUST), Wuhan 430074, People's Republic of China

[3] School of Energy and Power Engineering, Huazhong University of Science and Technology (HUST), Wuhan 430074, People's Republic of China

[4] Department of Aerospace and Mechanical Engineering, University of Notre Dame,

Notre Dame, Indiana 46556, USA.

[#] Z. J. and Q. L. contributed equally to this work.

* Corresponding authors: N.Y. (nuo@hust.edu.cn), H. F. (hafang@hust.edu.cn), and Z.L. (zcliu@hust.edu.cn)

I. Molecular dynamics (MD) simulation details

The lattice thermal conductivity of single-layer MoS_2 ($SLMoS_2$) is calculated by equilibrium molecular dynamics [S1]. Thermal conductivity is derived from the Green-Kubo formula [S2] as

$$\kappa = \frac{1}{3k_B T^2 V}\int_0^\infty < \vec{J}(\tau)\cdot\vec{J}(0) > d\tau \qquad \text{(S1)}$$

$$\vec{J}(\tau) = \sum_i \vec{v}_i \varepsilon_i + \frac{1}{2}\sum_{\mathrm{ij}\, i\neq j} \vec{r}_{ij}(\vec{F}_{ij}\cdot\vec{v}_i) + \sum_{ijk} \vec{r}_{ij}(\vec{F}_j(ijk)\cdot\vec{v}_j)$$

where κ is the thermal conductivity, k_B the Boltzmann constant, V the system volume, T the temperature, the angular bracket denoting ensemble average. $\vec{v}_i$, ε_i , and $\vec{r}_i$ are the velocity vector, the site energy, and the position vector of atom respectively. The distance between atom i and atom j is $\vec{r}_{ij} = \vec{r}_j - \vec{r}_i$. $\vec{F}_{ij}$ and $\vec{F}_j(ijk)$ denote the two-body and the three-body force, respectively.

The MD simulations are carried out utilizing LAMMPS software package [S3]. The Stillinger-Weber potential, whose parameters are fitted using GULP by Jiang *et al.* [S4], is adopted in our simulations (shown in Table S1). An appropriate empirical potential is fundamental to obtain a reliable MD calculation result. The phonon dispersion relations, which are extracted from two different empirical potentials for $SLMoS_2$, are compared with the results from DFT calculation, as shown in Fig. S1. The potential function used in this work provides a better reproduction of the phonon dispersion, which will assure a more reliable result on thermal conductivity.

Different from previous works on MoS_2 ribbons [S5], our MoS_2 model is a $SLMoS_2$ sheet. The periodic boundary conditions are applied along the two in-plane directions. There is no inter-

layer interaction due to the single layer structure. Therefore, in the simulations, the inter-layer van der Waals interactions are not taken into account. The two in-plane directions studied correspond to the armchair direction and the zigzag direction.

Generally, the temperature in MD simulation, T_{MD}, is calculated from the kinetic energy of atoms according to the Boltzmann distribution:

$$\langle E \rangle = \sum_{i=1}^{N} \frac{1}{2} m v_i^2 = \frac{3}{2} N k_B T_{MD} \tag{S2}$$

where $\langle E \rangle$ is the total kinetic energy, m the atomic mass, and N the number of particles in the system, respectively.

The velocity Verlet algorithm is employed to integrate equations of motion, and the time step is 0.5 fs. Initially, the Nose-Hoover heat reservoir is used to equilibrate the system at 300 K for 5×10^5 time steps (250ps). Then, simulations run in the *NPT* ensemble for 500 ps (10^6 time steps) to relax the structure. After relaxation, the converged values of both the cell size and the potential energy are obtained, which makes sure that there is no stress or strain effects. Then, the structure runs another 5 ns under NVE ensemble for relaxation. Now the system is ready for heat flux recording. The heat current vector is calculated and recorded each 2.5 fs for 8×10^6 time steps to obtain the autocorrelation function and thermal conductivity.

In Fig. S2, the black curve shows the normalized heat current autocorrelation function (HCACF) used in Green-Kubo formula to calculate thermal conductivity, where the side length of simulation cell is 8 units and the temperature is 300 K. Additionally, the blue curve shows the thermal conductivity which is an integration of the HFACF. The thermal conductivity converges

to 93.55 $Wm^{-1}K^{-1}$ after around 220 ps due to the decay of the HFACF. The final thermal conductivity is the mean value of twelve realizations with different initial conditions.

II. Finite size effect in simulations

When using Green Kubo formula to calculate thermal conductivity, the finite size effect could arise if the simulation cell is not sufficiently large [S2]. Fig. 4 shows the thermal conductivity of $SLMoS_2$ at room temperature with different cell sizes, from $2 \times 2 \times 1$ to $32 \times 32 \times 1$ $unit^3$. The thermal conductivity shows a strong dependence on the size when it's smaller than $8 \times 8 \times 1$ $unit^3$. However, it changes little when the size is larger. The simulation cell in our calculations is selected as large as $32 \times 32 \times 1$ $units^3$ ($34.7 \times 30.0 \times 0.616$ nm^3) which is large enough to overcome the finite size effect.

III. The anharmonic effects of the empirical potential function

In MD simulations, the inter-atomic potential parameters are fundamental to the accuracy of the thermal conductivity calculations. The inter-atomic potential parameters herein predict the thermal expansion coefficient to be 4.85×10^{-6} K^{-1} at room temperature, which is lower than the results of Huang *et al* [S6] and C. Sevik [S7] that is about 6.74×10^{-6} K^{-1} from the predictions of the first principles. It means that this empirical potential function somewhere underestimates the real anharmonicity and phonon-phonon scatterings. That is, the thermal conductivity would be overestimated in our work. Moreover, an overvalued thermal conductivity results in an underestimated *ZT*.

IV. Electron transport properties calculation details

We compared our DFT calculation in electron and phonon dispersion curves with previous results. Fig. S3 shows the electron and phonon band structures. The black solid lines are from our calculation, while the open square dots are the reference data coming from Ref. 22 of the main article. Our results agree well with the result in Ref. 22 of the main article.

The Boltzmann transport equation (BTE) is utilized to predict electronic transport properties. The assumptions, the constant relaxation time and the rigid band approximation[S8], are used in BTE calculation[S9]. These strategies in transport coefficients calculation have been verified through previous works[S8,S10]. With constant relaxation time assumption, transport coefficients for electrons can be obtained by

$$\sigma = \mathrm{L}^{(0)} \tag{S3}$$

$$S = -(1/eT)\sigma^{-1}\mathrm{L}^{(1)} \tag{S4}$$

$$\kappa_e = 1/(e^2T)\,(\mathrm{L}^{(2)} - \mathrm{L}^{(1)}\sigma\mathrm{L}^{(1)}) \tag{S5}$$

where $\mathrm{L}^{(\alpha)}$ is defined as :

$$\mathrm{L}^{(\alpha)} = e^2\tau\sum_n \int \frac{d\vec{k}}{4\pi^3}\left(-\frac{\partial f(\varepsilon_{n\vec{k}})}{\partial \varepsilon_{n\vec{k}}}\right)\overrightarrow{v_{n\vec{k}}}\overrightarrow{v_{n\vec{k}}}(\varepsilon_{n\vec{k}} - \mu)^{\alpha} \tag{S6}$$

where, $\varepsilon_{n\vec{k}}$ is the energy eigenvalue of the *n*th band at points in the first Brillouin zone, $f(\varepsilon_{n\vec{k}})$ the Fermi-Dirac distribution function at temperature T, μ the chemical potential, τ the

relaxation time and $\overrightarrow{v_{n\vec{k}}}$ the group velocity, respectively. Our calculations are focused on the in-plane transport coefficients of the two-dimensional structure. The Boltzmann equation for transport coefficients is solved by BoltzTrap [S9].

The relaxation time is a key parameter in solving Boltzmann equation. For electronic transport in semiconductor, the relaxation time is mostly affected by scatterings, such as impurity, boundary, and phonons. The relationship between the relaxation time and mobility (μ) is defined as $\tau=m^*\mu/e$, where m^* is the effective mass. We get the average values of effective mass, $0.50m_0$ for electrons and $0.64m_0$ for holes, where m_0 is the mass of electron. That is, we can obtain the relaxation time based on the mobility.

Kim *et. al* predicted the mobility in MoS_2 both theoretically and experimentally [S11]. It shows that the experimental results are consistent with the theoretical predictions. In their theoretical model, the impurity scatterings, acoustic phonon scatterings, and optical scatterings are all taken into consideration, which produces comprehensive results. Therefore, their values of mobility are used in our calculation. However, they provide values of mobility below 300 K only. We obtain the mobility for higher temperature according to the reciprocal relationship[S12,S13]. The values of mobility for 300 K, 400 K and 500 K are fitted as 180.27 $cm^2V^{-1}s^{-1}$, 117.55 $cm^2V^{-1}s^{-1}$ and 79.92 $cm^2V^{-1}s^{-1}$, respectively. Besides, based on the results from Kaasbjerg *et. al* [S12], the mobility is not sensitive to carrier concentration. Therefore, it is assumed that the mobility and relaxation time are independent on the concentration in our calculation.

The relaxation time of n-type $SLMoS_2$ for 300 K, 400 K, and 500 K are fitted as 5.17×10^{-14} s, 3.37×10^{-14} s and 2.29×10^{-14} s, respectively. The values are in the range of the prediction based on deformation potential theory by Fan *et al*.[S14].

V. Thermoelectric property

With the calculated band structures, we can obtain the transport tensor of $SLMoS_2$. In Fig. S5, there is little difference for Seebeck coefficients along two in-plane orthogonal directions, x and y. So, average values are taken and the $SLMoS_2$ is treated as isotropic here.

As the Fermi level shifts from band gap to valence band, we can get the transport properties under p-type carrier concentration with rigid band approximation. Fig. S6 shows the thermoelectric properties when $SLMoS_2$ is p-type doped. Compared with the results of *ZT* for n-type $SLMoS_2$ (shown in Fig. 3), the p-type has smaller *ZT* values, because the n-type has bigger Seebeck coefficients.

REFERENCES

S1. Hoover, W. G. *et al.* Lennard-Jones triple-point bulk and shear viscosities. Green-Kubo theory, Hamiltonian mechanics, and nonequilibrium molecular dynamics. *Phys. Rev. A* **22**, 1690-1697, doi:10.1103/PhysRevA.22.1690 (1980).

S2. Yang, L. N., Yang, N. & Li, B. W. Reduction of Thermal Conductivity by Nanoscale 3D Phononic Crystal. *Sci Rep* **3**, 1143, doi:10.1038/Srep01143 (2013).

S3. Plimpton, S. Fast Parallel Algorithms for Short-Range Molecular Dynamics. *J. Comput. Phys.* **117**, 1-19, doi:10.1006/jcph.1995.1039 (1995).

S4. Jiang, J. W., Park, H. S. & Rabczuk, T. Molecular dynamics simulations of single-layer molybdenum disulphide (MoS2): Stillinger-Weber parametrization, mechanical properties, and thermal conductivity. *J. Appl. Phys.* **114**, 064307, doi:10.1063/1.4818414 (2013).

S5. Jiang, J. W., Zhuang, X. Y. & Rabczuk, T. Orientation Dependent Thermal Conductance in Single-Layer MoS2. *Sci Rep* **3**, 4, doi:10.1038/srep02209 (2013).

S6. Huang, L. F., Gong, P. L. & Zeng, Z. Correlation between structure, phonon spectra, thermal expansion, and thermomechanics of single-layer MoS2. *Phys. Rev. B* **90**, 045409, doi:10.1103/PhysRevB.90.045409 (2014).

S7. Sevik, C. Assessment on lattice thermal properties of two-dimensional honeycomb structures: Graphene, h-BN, h-MoS2, and h-MoSe2. *Phys. Rev. B* **89**, 035422, doi:10.1103/PhysRevB.89.035422 (2014).

.

S8. Lee, M. S. & Mahanti, S. D. Validity of the rigid band approximation in the study of the thermopower of narrow band gap semiconductors. *Phys. Rev. B* **85**, doi:10.1103/PhysRevB.85.165149 (2012).

S9. Madsen, G. K. H. & Singh, D. J. BoltzTraP. A code for calculating band-structure dependent quantities. *Comput Phys Commu* **175**, 67-71, doi:10.1016/j.cpc.2006.03.007 (2006).

S10. Huang, B.-L. & Kaviany, M. Ab initio and molecular dynamics predictions for electron and phonon transport in bismuth telluride. *Phys. Rev. B* **77**, 125209, doi:10.1103/PhysRevB.77.125209 (2008).

S11. Kim, S. *et al.* High-mobility and low-power thin-film transistors based on multilayer MoS2 crystals. *Nat. commun.* **3**, 1101, doi:10.1038/ncomms2018 (2012).
S12. Kaasbjerg, K., Thygesen, K. S. & Jacobsen, K. W. Phonon-limited mobility in n-type single-layer MoS2 from first principles. *Phys. Rev. B* **85**, 115317, doi:10.1103/PhysRevB.85.115317 (2012).
S13. Kawamura, T. & Das Sarma, S. Phonon-scattering-limited electron mobilities inAlxGa1−xAs/GaAs heterojunctions. *Phys. Rev. B* **45**, 3612-3627, doi:10.1103/PhysRevB.45.3612 (1992).
S14. Fan, D. D. *et al.* MoS2 nanoribbons as promising thermoelectric materials. *Appl. Phys. Lett.* **105**, 133113, doi:10.1063/1.4897349 (2014).

Table S1. Stillinger-Weber potential parameters used in MD simulations. The two-body potential expression is $V_2 = \varepsilon A(B\sigma^p r_{ij}^{-p} - \sigma^q r_{ij}^{-q}) e^{[\sigma(r_{ij}-a\sigma)^{-1}]}$. The three-body potential expression is $V_3 = \varepsilon\lambda e[\gamma\sigma(r_{ij}-a\sigma)^{-1} + \gamma\sigma(r_{jk}-a\sigma)^{-1}](\cos\theta_{jik} - \cos\theta_0)^2$. Energy parameters are in the unit of eV. The parameters of size are in the unit of Å.

	ε	σ	a	λ	γ	cos θ_0	A	B	p	q	tol
Mo-S-S	6.0672	0.7590	4.1634	1.0801	0.8568	0.1525	1.0	45.4357	4	0	0.0
S-Mo-Mo	6.0672	0.7590	4.1634	1.0801	0.8568	0.1525	1.0	45.4357	4	0	0.0
Mo-Mo-Mo	3.5040	0.6097	7.0034	0.0	0.0	0.0	1.0	181.8799	4	0	0.0
S-S-S	0.4651	0.6501	5.7837	0.0	0.0	0.0	1.0	125.0923	4	0	0.0

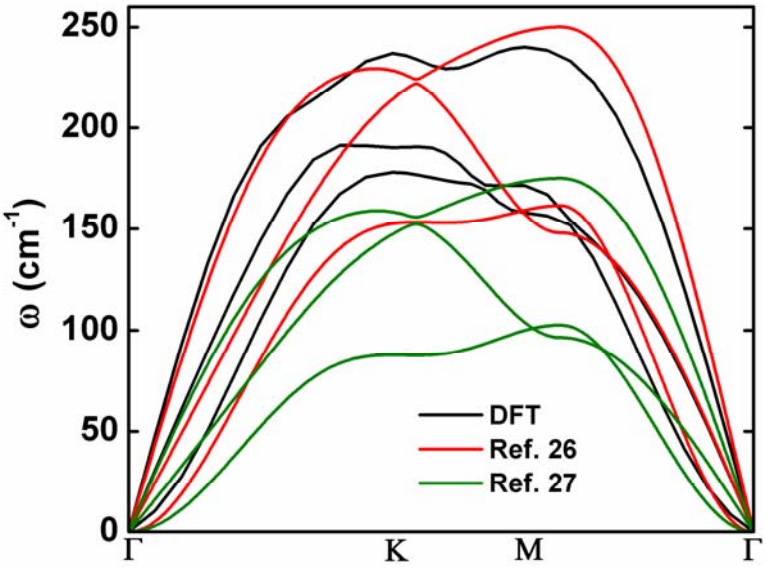

Fig. S1 The comparison of the acoustic phonon dispersion curves from DFT and the empirical potential functions implemented in Ref. 26 and Ref. 27 of the main article.

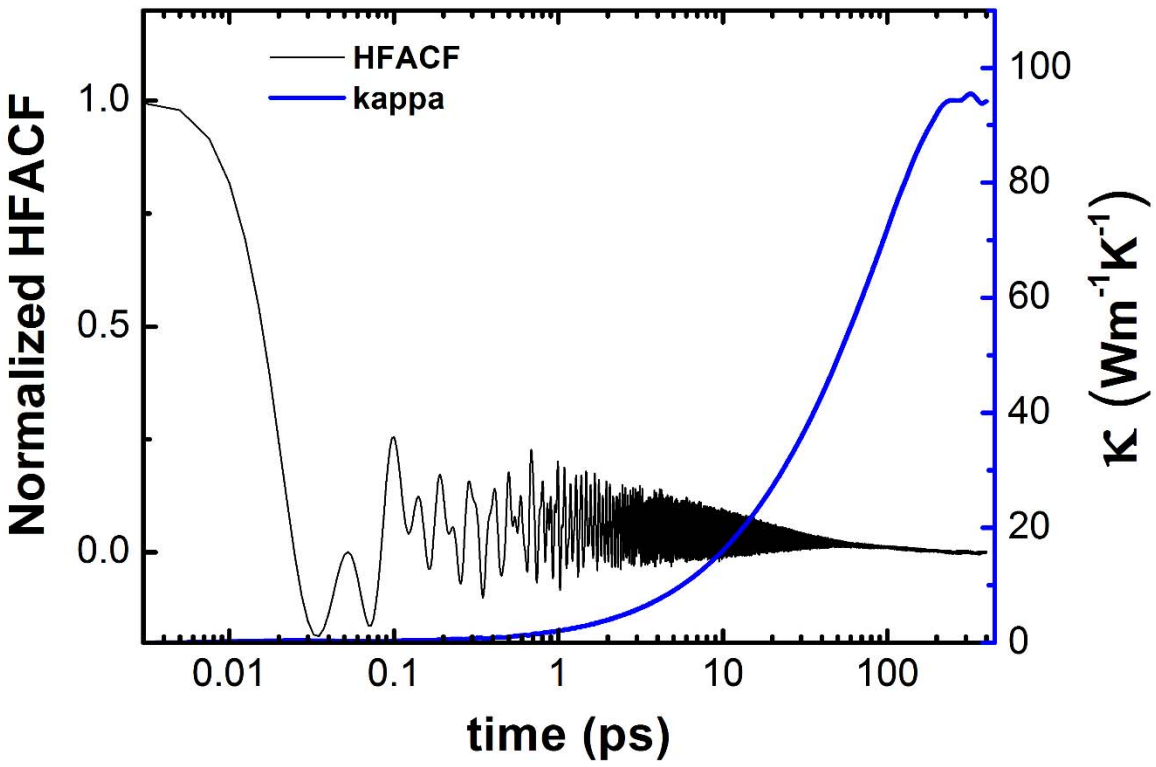

Fig. S2 The Normalized heat flux autocorrelation function (HFACF) and thermal conductivity (κ) along the y direction of $SLMoS_2$ versus correlation time. The side length of simulation cell is 8 units. The figure shows, after 220 ps, the HFACF decays close to zero and the thermal conductivity converges.

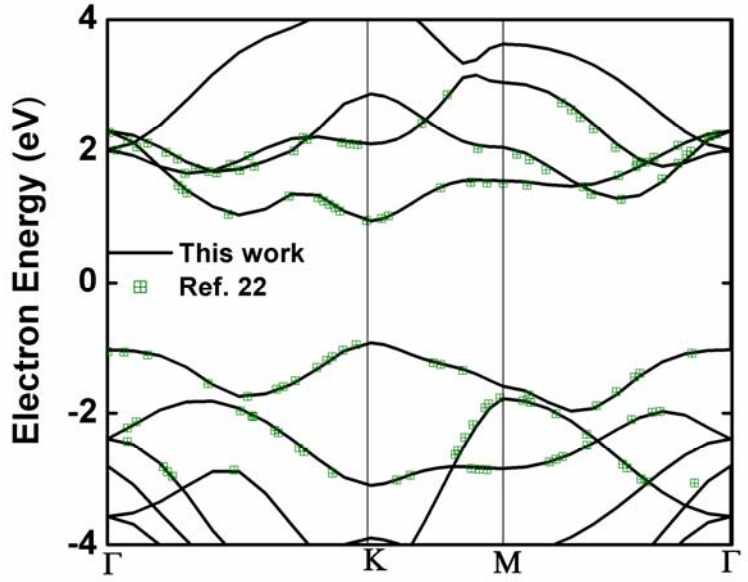

(a)

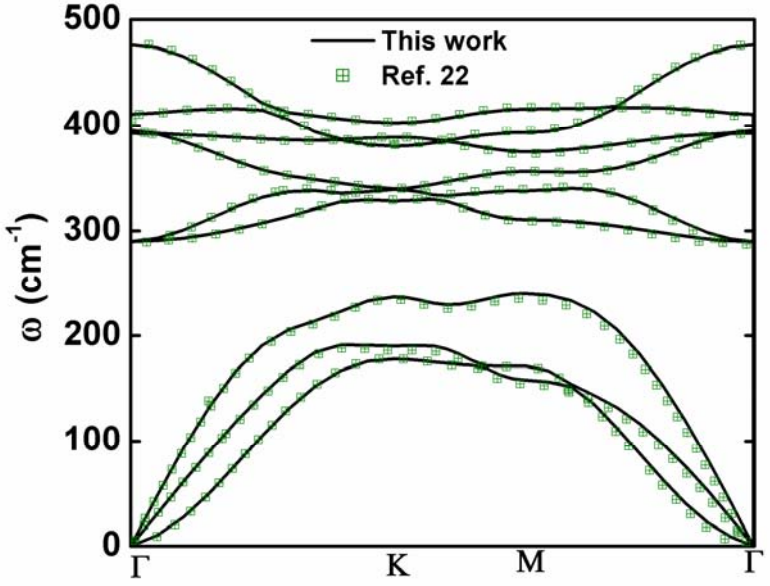

(b)

Fig. S3 (a) The electron band structures come from our calculation and those in Ref. 22 of the main article. (b) The phonon dispersion curves come from our calculation and those in Ref. 22 of the main article.

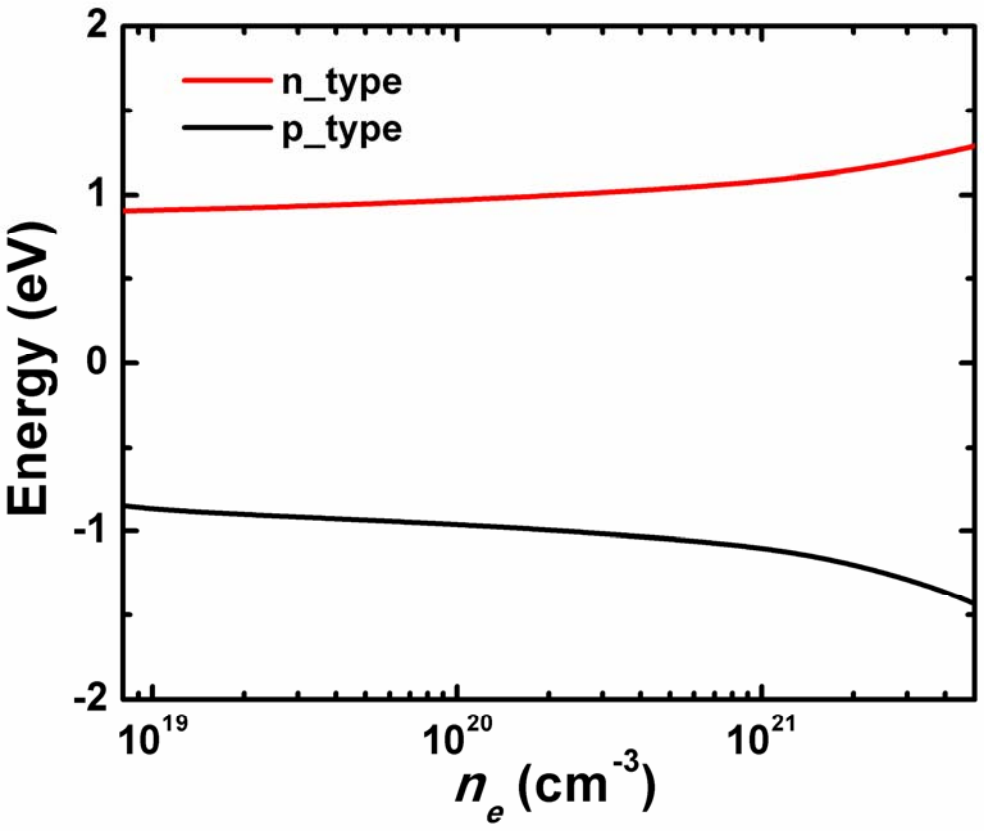

Fig. S4 The chemical potential versus the carrier concentration.

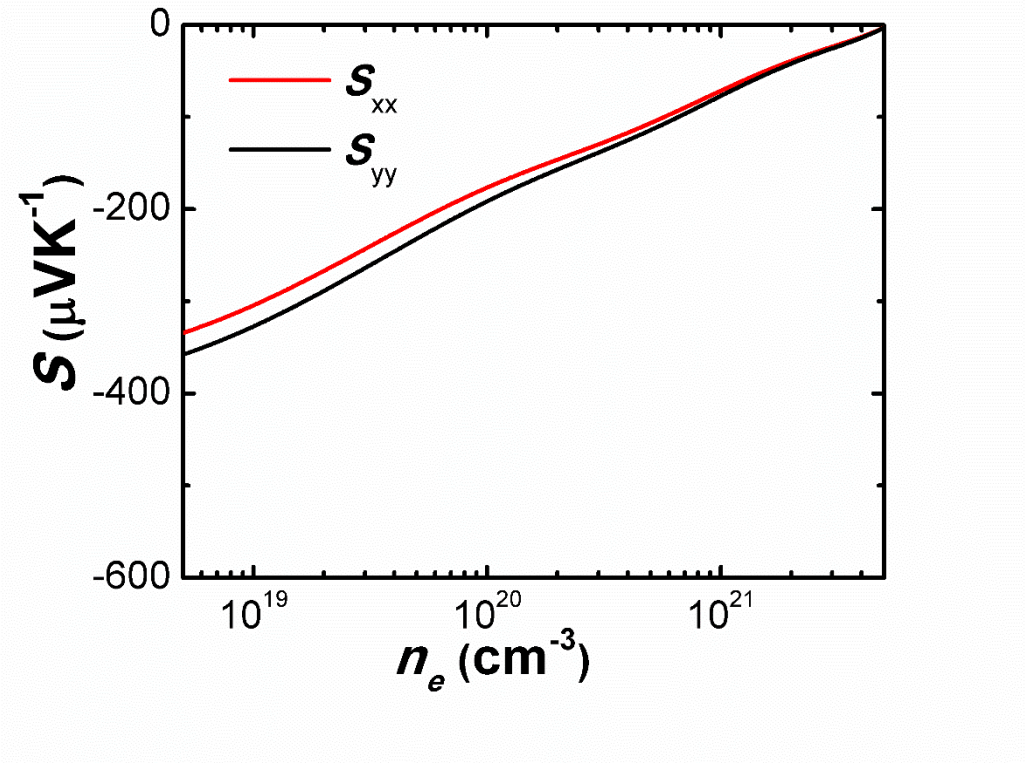

Fig. S5 The Seebeck coefficients of $SLMoS_2$ along two in-plane orthogonal directions, x and y. .

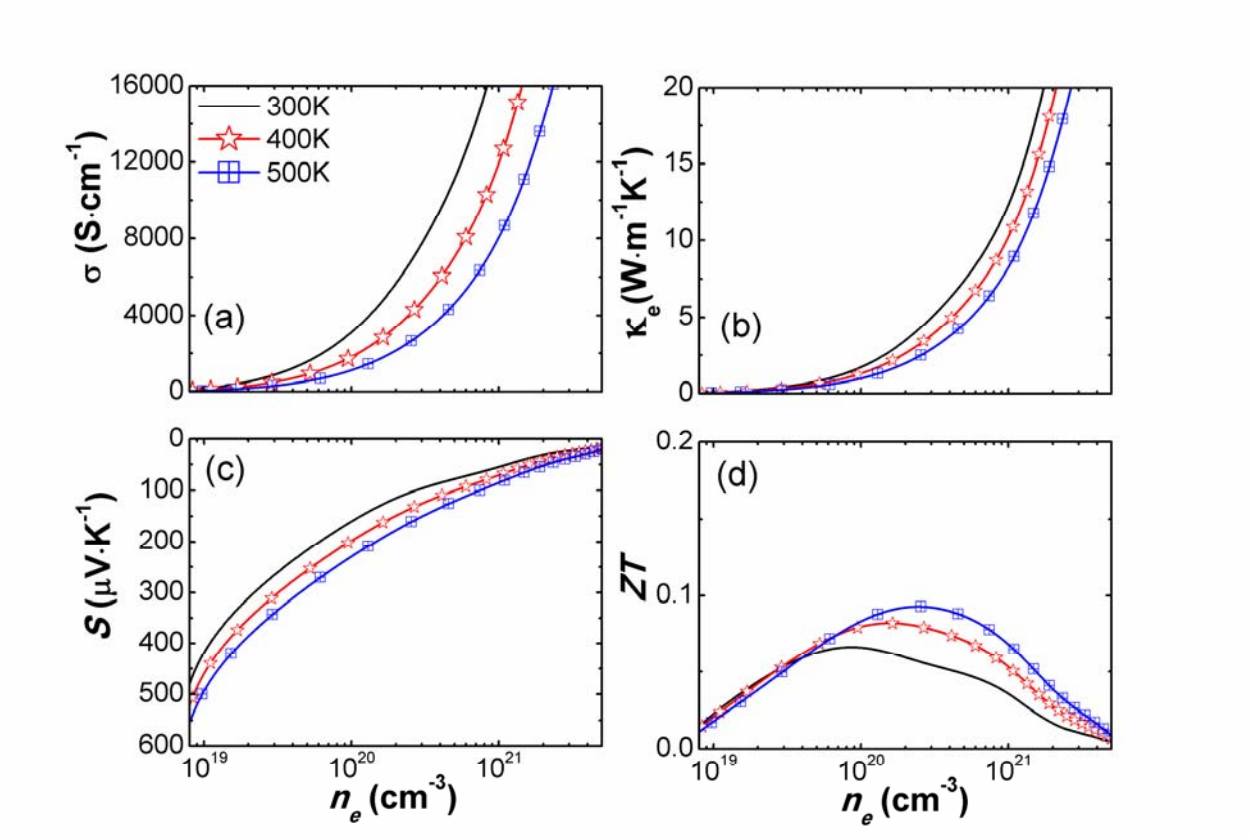

Fig. S6 The thermoelectric transport properties of p-type $SLMoS_2$ at 300 K, 400 K and 500 K. (a) The electrical conductivity; (b) The electronic thermal conductivity; (c) The Seebeck coefficient; (d) The figure of merit.